Journal of Materials Chemistry A

Lithium–Sulfur Full Cell Exceeding 4000 Cycles: Influence of Tailored Cathode Structure and Polysulfide Additive

Journal:	*Journal of Materials Chemistry A*
Manuscript ID:	TA-ART-12-2014-006748
Article Type:	Paper
Date Submitted by the Author:	09-Dec-2014
Complete List of Authors:	Thieme, Sören; Fraunhofer, IWS Brückner, Jan; Fraunhofer, IWS Meier, Andreas; Dresden University of Technology, Institute of Inorganic Chemistry Bauer, Ingolf; Fraunhofer, IWS Gruber, Katharina; Varta Micro Innovation GmbH, Kaspar, Jörg; Fraunhofer, IWS Helmer, Alexandra; Fraunhofer, IWS Althues, Holger; Fraunhofer, IWS Schmuck, Martin; Varta Micro Innovation GmbH, Kaskel, Stefan; Fraunhofer, IWS; Dresden University of Technology, Institute of Inorganic Chemistry

SCHOLARONE™
Manuscripts

Lithium-Sulfur Full Cell with Ultralong Cycle Life: Influence of Cathode Structure and Polysulfide Additive

Sören Thieme[1], Jan Brückner[1], Andreas Meier[2], Ingolf Bauer[1], Katharina Gruber[3], Jörg Kaspar[1], Alexandra Helmer[1], Holger Althues[1], Martin Schmuck[3], and Stefan Kaskel[1,2,]*

[1] *Fraunhofer Institute for Material and Beam Technology, Winterbergstraße 28, D-01277 Dresden, Germany*

[2] *Department of Inorganic Chemistry, Dresden University of Technology, Bergstraße 66, D-01062 Dresden, Germany*

[3] *VARTA Micro Innovation GmbH, Stremayrgasse 9, A-8010 Graz, Austria*

*Corresponding author. Phone: +49-35146333632; E-mail: stefan.kaskel@chemie.tu-dresden.de

Abstract

Lithium-sulfur batteries are highly attractive energy storage systems, but suffer from structural anode and cathode degradation, capacity fade and fast cell failure (dry out). To address these issues, a carbide-derived carbon (DUT-107) featuring a high surface area (2088 m^2 g^{-1}), high total pore volume (3.17 cm^3 g^{-1}) and hierarchical micro-, meso- and macropore structure is applied as rigid scaffold for sulfur infiltration. The DUT-107/S cathodes combine excellent mechanical stability and high initial capacities (1098 – 1208 mAh g^{-1}_S) with high sulfur content (69.7 wt% per total electrode) and loading (2.3 – 2.9 mg$_S$ cm^{-2}). Derived from the effect of the electrolyte-to-sulfur ratio on capacity retention and cyclability, conducting salt is substituted by polysulfide additive for reduced polysulfide leakage and capacity stabilization. Moreover, in a full cell model system using a prelithiated hard carbon anode, the performance of DUT-107/S cathodes is demonstrated over 4100 cycles (final capacity of 422 mAh g^{-1}_S) with a very low capacity decay of 0.0118 % per cycle. Application of PS additive further boosts the performance (final capacity of 554 mAh g^{-1}_S), although a slightly higher decay of 0.0125 % per cycle is observed.

1. Introduction

Lithium-sulfur (Li-S) batteries are one of the most promising next generation energy storage systems for highly demanding applications in consumer electronics and electromobility. Advantageous properties of the Li-S system are the abundance, low cost and eco-friendliness of sulfur as well as an intrinsic overcharge protection. These are immense economic and ecological benefits over state-of-the-art lithium-ion battery technology. Moreover, according to optimistic estimates, a doubling of the gravimetric energy density will be possible.[1,2] This is because of the high theoretical capacity of 1672 mAh g^{-1}_S of the underlying conversion of sulfur to lithium sulfide (Li_2S) in combination with an average cell voltage of 2.15 V. However, the wide-spread commercialization of Li-S batteries can only be achieved if fundamental issues are resolved. They are related not only to the complex multi-step conversion of sulfur to Li_2S and vice versa, but also to the thermodynamic instability of elemental lithium. One of these problems arises from the high solubility of reaction intermediates (polysulfide; PS) in the electrolyte.[3] Although necessary for fast reaction kinetics and high sulfur utilization,[2,4,5] this process inevitably leads to active material loss through irreversible sulfur extraction from the cathode.[6,7] In addition it causes a PS shuttle leading to low shelf life and lithium corrosion.[8,9,10,11] Simultaneously, the repeated dissolution and deposition of active material accompanied by volume change degrades the porous cathode structure.[12–14] This deteriorates not only the conductivity of the carbon scaffold but also the charge transfer kinetics due to formation of insulating layers.[4,12,15] Another problem is the structural degradation of the anode caused by dendrite formation and mossy-like lithium growth upon repeated cycling.[8,16] This process increases the surface area and, thus, accelerates the reactions with PS, $LiNO_3$ and organic solvents at the instable lithium/electrolyte interface. Consequently, cycling of Li-S batteries at stable capacities over hundreds of cycles is highly challenging. This is even more pronounced in cells comprising sulfur cathodes with high sulfur loading and content as well as a low amount of electrolyte.[11,17–20]

After the pioneering work of the Nazar group using mesoporous carbon (CMK-3) as host structure,[6] research focused heavily on the rational design of carbon materials. These materials exhibit micro-, meso- and macropores in order to achieve improved PS (capacity) retention as well as fast reaction kinetics even at high sulfur content in the cathode. Although preparation and measurement conditions are diverse, the conclusion was drawn that high surface area micropores improve the electrical contact to insulating sulfur. Therefore, they effectively contribute to the adsorption of PS allowing for stable cycling at high capacity (1000 – 1350 mAh g^{-1}_S; < 55 wt% sulfur in composite).[21] At the same time meso- and macropores, respectively, are required to overcome limitations such as mass transport restriction, pore blocking and low sulfur content. Hierarchical structured carbons satisfy the requirements and, therefore, effective cathodes with initial capacities of 700 – 1400 mAh g^{-1}_S (50 – 84 wt% sulfur in composite) were reported.[22–31] Nevertheless, PS leakage was still observed due to the relative weak adsorption of PS in these open-pore systems.

A recent approach by the Cui group demonstrated an elaborated sulfur-TiO_2 yolk-shell nanoarchitecture, which showed stable performance and low capacity decay of 0.033 % per cycle over 1000 cycles.[32] Moreover, a reversible operation up to 1500 cycles with decay of 0.043 % per cycle was achieved by Lui and co-workers, who constructed a hybrid structure by wrapping graphene around sulfur-impregnated carbon nanofibers.[33] Notably, the application of alternative anodes as substitute for lithium is also a promising approach.[34] A recent publication by our group demonstrated long-lasting performance over more than 1300 cycles combined with a decay of only 0.08 % per cycle.[35]

In this paper, we report the application of a conductive carbide-derived carbon (CDC) material (DUT-107) with a hierarchical micro-, meso- and macropore structure. The high pore volume enables a high sulfur content of 82 wt% in the composite, while at the same time initial capacities in range of 1098 to 1208 mAh g^{-1}_S can be achieved in a half cell setup (vs. lithium). The capacities are almost independent from the amount of electrolyte (5.0 – 12.0 µL

mg^{-1}$_S$) used. Moreover, the substitution of conducting salt by PS additive resulted in reduced PS leakage and capacity stabilization. Finally, inspired by the successful application of prelithiated hard carbon as stable anode, we used a full cell model system to demonstrate ultralong, reversible cycling over 4100 cycles. The capacity decay is only 0.0118 % per cycle (final capacity of 422 mAh g^{-1}$_S$). Application of PS additive resulted in a further performance boost by 31% (final capacity of 554 mAh g^{-1}$_S$).

2. Results and Discussion

2.1. Characterization of DUT-107 and DUT-107/S composite structure

The pore structure and rigidity of the carbon material as well as the sulfur distribution in the composite have a strong influence on the conversion kinetics, sulfur utilization and long-lasting mechanical stability of sulfur cathodes. Therefore, making a detailed structural investigation of our here reported CDC (DUT-107) and its composite (DUT-107/S) is essential.

The nitrogen physisorption (-196 °C) isotherm of DUT-107 (Figure 1a) clearly shows its multimodal pore characteristics. There, the high amount of nitrogen adsorbed in the low-pressure region is associated with the filling of narrow micropores generated by silicon extraction. Further, the continuous increase of nitrogen uptake in the mid-pressure region combined with a hysteresis loop (for $p/p_0 > 0.44$) evidences the presence of irregular sized mesopores. In contrast to typical type IV isotherms usually observed for ordered mesoporous CDC materials,[36,37] DUT-107 exhibits a steep increase of the nitrogen adsorption at $p/p_0 > 0.9$ indicating the presence of large meso- and macropores. Accordingly, the pore size distribution (PSD, Figure 1b) reveals a high share of micropores ($d_P < 2$ nm) in DUT-107 significantly contributing to its high specific surface area of 2088 m^2 g^{-1}. The micropore volume is 0.50 cm^3 g^{-1}. Moreover, several peaks are observed in the PSD for pores in the 2 – 32 nm range evidencing an irregular mesopore size. This results from the presence of large mesopores (d_P

> 6 nm) introduced by the silica-template as well as small mesopores (2 nm < d_P < 6 nm) located in the pore walls. Since nitrogen physisorption is inadequate for the characterization of large meso- and macropores, mercury intrusion porosimetry was also applied. The intrusion curve (Figure 1c) shows that DUT-107 bulk powder can take up high amounts of mercury over a wide pore diameter range. However, this effect is not attributable solely to the internal porosity of individual DUT-107 particles but also to inter-particular pores. This can be concluded from the corresponding HG-PSD (Figure 1c inset) showing a small peak for small mesopores (d_P < 10 nm) as well as a broad peak with four pronounced maxima in the meso- to macropore region (10 nm < d_P < 200 nm), which is also in agreement with the nitrogen physisorption data. Moreover, several peaks are observed for very large pores (d_P > 500 nm) whose diameter even exceeds the DUT-107 particle size. Consequently, these pores are considered as inter-particular voids. By combining the nitrogen pore volume (0.81 cm^3 g^{-1} for pores with d_P ≤ 5.56 nm) and the intruded mercury volume (2.36 cm^3 g^{-1} for pores with 5.67 nm < d_P < 192.29 nm) the total pore volume of DUT-107 was calculated to be 3.17 cm^3 g^{-1}.

In comparison to DUT-107, the nitrogen physisorption isotherm of the DUT-107/S composite (Figure 1a) shows only low adsorption of nitrogen in the low- to mid-pressure region as well as a shift of the hysteresis loop to high relative pressure (p/p_0 > 0.81). This is consistent with the preferable sulfur infiltration in micro- as well as small mesopores located in the pore walls due to strong interaction. In contrast, large meso- and macropores remain almost unfilled, which is indicated by the steep increase of the nitrogen adsorption at p/p_0 > 0.9 observed for both DUT-107 and DUT-107/S. Further evidence is provided by the corresponding PSD showing that both micro- and small mesopores (d_P < 6 nm) nearly vanish, whereas large pores (d_P > 20 nm) are less affected by sulfur infiltration. In the range of 6 – 20 nm not only a decreased intensity but also a shift to smaller pore diameters is observed for DUT-107/S compared to DUT-107. This indicates the coating of mesopore walls with sulfur, which is in

agreement with the hysteresis loop shift. The adjustment of sulfur localization in the pore walls under retention of free transport pores is essential for an improved cathode performance. This enables fast kinetics, unhindered mass transport, wettability, and PS storage in close distance to the reaction sites even at high sulfur content. In this regard, it is important to point out the special role of DUT-107. With its multimodal hierarchical pore structure and high pore volume, it allows for a high sulfur content of 82 wt% in the DUT-107/S composite according to TG analysis (Figure 1d). This value is in good agreement with the adjusted DUT-107-to-sulfur ratio of 1:4 (by weight). Compared to pristine sulfur and sulfur in DUT-107/S, the DUT-107 material shows a high thermal stability with no significant weight loss up to 450 °C in air atmosphere. It is further characterized by a high purity (< 1 wt% residue at 800 °C).

The TEM and SEM studies of a typical DUT-107 particle, support the nitrogen physisorption as well as mercury intrusion porosimetry results and, thus, indicate the existence of a multimodal hierarchical pore structure. According to the TEM image (Figure 1e) the internal porosity of the DUT-107 particle is the replica of the silica-template (Figure S1a). Thus, it mainly consists of sphere-like shaped, large mesopores of irregular size enwrapped by a thin carbon wall. Moreover, the defects observed in part of these pore walls result in the association of individual mesopores under formation of irregular shaped macropores ($d_P > 50$ nm). It is further observed that the mesopore walls consist of small, agglomerated carbon rods with irregular orientation (Figure S1b) and, as evidenced by nitrogen physisorption, include micropores as well as small mesopores (2 – 6 nm range). Additionally, SEM images (Figure 1f and S1c) show the topography of the typical DUT-107 particle. The outer appearance of the particle is characterized by a rough surface as well as large, spherical pores with up to 200 nm diameter generating the open, hierarchical pore structure. Interestingly, both the pore structure and the outer shape (rough topography) of the DUT-107 particle is not changed by sulfur infiltration as can be concluded from the SEM image (Figure 1g and S1d) of the DUT-

107/S composite. This indicates that sulfur is completely included in the internal pores of DUT-107. A formation of layers or agglomerates covering the particle surface is not visible. SEM further reveals that the large meso- and macropores are maintained in DUT-107/S, whereas the micro- and small mesopores located in the pore walls of DUT-107 are covered with a thin sulfur film. This finding supports the results obtained from nitrogen physisorption of DUT-107/S and shows the formation of a mechanically stable scaffold suited to withstand pressure differences and volume change caused by the electrochemical sulfur conversion.

2.2. Structural characterization of DUT-107/S cathodes

Cathode samples with sulfur content of 69.7 wt% per total electrode and sulfur loading of 2.3 – 2.9 mg_S cm^{-2} were prepared from the DUT-107/S composite powder. These parameters can address both of the so called "two lows",[38,39] which became an important subject to recent literature since it was realized that practically relevant, high capacity cathodes not only require high performance but also a reasonable sulfur content and loading. This is in considerable contrast to numerous material approaches, which are focused heavily on the maximization of the sulfur utilization, rate capability and cycling stability, but make use of ideal measurement conditions (application of thin films with low loading or cathodes with insufficient sulfur content).[1,11,18,23,24,32,33,39,40] In these systems the cathode kinetics are optimal due to fast electron transfer and unrestricted Li ion diffusion throughout the thin active layer even if the electrolyte is enriched with dissolved PS (viscosity increase). Moreover, the cycling stability largely benefits from stripping and plating only small amounts of lithium.[2,8] According to XRD (Figure 2a) nano-sized sulfur is well confined inside the pore structure of DUT-107. Hence, only two weak sulfur peaks (solid lines) are observed for the as-prepared DUT-107/S cathode. The other peaks, in contrast, are assigned to the current collector (dotted lines) as well as graphitic domains of DUT-107 (dashed lines) as can be concluded from reference measurements (Figure S2).

Due to repeated forming and pressing during preparation by solvent-free roll pressing, the DUT-107/S cathode possesses a smooth and crack-free surface as visible in the SEM image (Figure 2b). However, also inter-particular macropores remain in the active layer consisting of DUT-107/S particles typically smaller than 5 μm. This is essential to assure the homogeneous wetting with electrolyte. According to the BSE-SEM image (Figure S3a) showing an excellent contrast for heavy elements, the sulfur is concentrated inside the pores of individual DUT-107 particles. The inter-particular room is filled with a flexible, persistent 3D conductive MWCNT network (Figure S3b). Relating to the active layer this generates a homogeneous sulfur distribution as evidenced by EDX elemental mapping (Figure 2c).

The cathode morphology combining persistent mechanical stability with intimate electrical contact presents a good scaffold for long-lasting cyclability. Thus, according to the SEM image (Figure 2d) of a charged DUT-107/S cathode cycled with reference electrolyte (R-E; 1 M LiTFSI + 0.25 M LiNO$_3$ in DME/DOL), neither structural degradation nor formation of passivating sulfur agglomerates or layers occurred. Cracks or delaminated DUT-107/S particles are not observed, however, the inter-particular macropores appear slightly compacted, which may be attributed to the high pressure applied on the cathode in the coin cell. Even the increase of reversible sulfur utilization caused by the application of polysulfide electrolyte (PS-E; 0.8 M LiTFSI + 0.25 M LiNO$_3$ + 0.15 M Li$_2$S$_6$ in DME/DOL) does not change the cathode structure in charged state (Figure 2f). As is evidenced by the lack of sulfur peaks in the XRD pattern of charged DUT-107/S cathodes cycled with R-E and PS-E, respectively, sulfur is still confined in the pores of DUT-107. Cracks and active material agglomeration are also not observed for discharged cathodes cycled with R-E (Figure 2e) and PS-E (Figure 2g), respectively. Although the inter-particular macropores look compacted, the high resolution SEM image (Figure S3c) of a cathode cycled with R-E reveals the preservation of accessibility. In contrast, the porosity is decreased when using PS-E indicating the deposition of higher amounts of Li$_2$S in the cathode due to increased active material

utilization. Although the cathode surface looks compacted, pores of reduced diameter are still visible at high resolution (Figure S3d). In the corresponding XRD pattern of the discharged cathodes no Li_2S peaks are observed for both R-E and PS-E, indicating that nano-confinement inside the multimodal, hierarchical structured pores of DUT-107 also applies to the discharge product. This is in clear contrast to studies performed with carbon black based sulfur cathodes, where Li_2S was detected due to particle nucleation and growth (agglomeration).[13,41] The comparison underlines the importance of DUT-107 as a rigid scaffold with high pore volume and surface area for reversible and locally confined active material transformation.

2.3. Electrochemical characterization of DUT-107/S cathodes in half cells (Li-S)

Using R-E initial capacities in range of 1098 to 1208 mAh g^{-1}_S were measured for the DUT-107/S cathodes (Figure 3a) being comparable to recent literature applying hierarchical porous carbon as sulfur host.[22,24–31] However, as mentioned previously, the DUT-107/S cathodes presented here surpass these material approaches in terms of sulfur content and loading. Moreover, in contrast to reports highlighting the importance of applying high amounts of electrolyte in half cells (exceeding 7 µL mg^{-1}_S) to achieve good performance and reproducible results,[2,11,19,20] the initial capacity of the DUT-107/S cathodes cycled at 0.1 C is relatively independent from the applied E/S ratio, which can even be 5.0 µL_{R-E} mg^{-1}_S. Accordingly, no voltage drop is observed in the upper plateau (conversion of sulfur to long chain PS) of the discharge voltage profiles of DUT-107/S cathodes (Figure 3b). Moreover, only a slight depression of the lower plateau (conversion of PS to Li_2S_2/Li_2S) was observed for low E/S ratios of 5.0 and 6.5 µL_{R-E} mg^{-1}_S indicating low polarization. This is caused not only by the improved electrical contact to insulating sulfur embedded in the micro- and small mesopores of DUT-107 but also by a minimized impact of the electrolyte resistance change. The latter is essential considering that the dissolution of PS increases the electrolyte viscosity and therefore reduces its ionic conductivity.[4,10,11] The issue becomes more severe at low E/S

ratios, but can be addressed by the hierarchical pore structure of DUT-107. It provides PS

reservoirs (large meso- and macropores), in which dissolved PS are concentrated, in close

distance to the high surface area reaction sites (micro- and small mesopores located in pore

walls), which maximize the interface to the electrolyte. Due to the thus reduced diffusion

length of active species, the sensitivity to viscosity change is minimized in the DUT-107/S

composite. This is a considerable advantage over non-hierarchical structured materials, in

which dissolved PS are forced to cover long distances to reach the next active reaction site.

Moreover, the Li ion accessibility of the DUT-107/S particles is excellent since mass

transport through large pores is unrestricted. An initial capacity of 1098 mAh g^{-1}_S and stable

capacity of 901 mAh g^{-1}_S was obtained for the DUT-107/S cathode and 5.0 μL_{R-E} mg^{-1}_S

corresponding to a capacity retention of 82.1 % (Figure 3d) over 50 cycles. Nevertheless, both

discharge capacity and coulombic efficiency (CE) suddenly dropped afterwards. This

indicates the complete consumption of the $LiNO_3$ inevitably leading to the formation of an

instable solid electrolyte interface (SEI) on the lithium anode. As a consequence, this causes

anode failure due to severe shuttle (lithium corrosion and accelerated growth of insulating

layers) as well as electrolyte depletion. As can be deduced from the cycling experiments

performed with higher amounts of R-E for up to 200 cycles (Figure 3a), the E/S ratio has a

two-fold impact. First, a higher E/S allows for longer cycling since the total amount of $LiNO_3$,

which scales linearly with the applied electrolyte volume, is increased. Moreover, detrimental

effects such as electrolyte depletion are masked by the high solvent excess. Second, a higher

E/S ratio leads to an increased gap between the initial and stable capacity as is reflected by the

capacity retention after 50 cycles (Figure 3d). Whereas 82.1 % are retained for an E/S ratio of

5.0 μL_{R-E} mg^{-1}_S, the value decreases to 71.6 % for 6.5 (initial: 1164 mAh g^{-1}_S; stable: 834

mAh g^{-1}_S), 64.0 % for 8.0 (initial: 1182 mAh g^{-1}_S; stable: 757 mAh g^{-1}_S) and 55.2 % for 12.0

μL_{R-E} mg^{-1}_S (initial: 1208 mAh g^{-1}_S; stable: 667 mAh g^{-1}_S). However, once the half cell is

equilibrated the capacity remains stable until cell failure is observed after 50 (E/S = 5.0), 100

(E/S = 6.5), 150 (E/S = 8.0) and more than 200 cycles (E/S = 12.0). This result is consistent with a report by Urbonaite et al., who found that fading was accelerated in a half cell comprising a low amount of electrolyte (E/S ca. 13), although the capacity retention in the first cycles was improved.[20]

In previous reports, the initial capacity drop was often associated with the dissolution of sulfur residues covering the composite particle surface.[6,24] However, the clear correlation between E/S ratio and capacity drop during cell equilibration suggests that PS are dissolved in the electrolyte until a saturated (equilibrium) state is reached. Accordingly, a precise adjustment of the PS concentration in the electrolyte (pre-saturation) may help in suppressing irreversible losses.[42] For this reason 0.2 M LiTFSI conducting salt was substituted by 0.15 M Li_2S_6 giving the PS-E. The impact on the capacity retention is clearly visible (Figure 3c) since a DUT-107/S cathode cycled with PS-E and E/S ratio of 12 μL_{PS-E} mg^{-1}_S provides a stable capacity of 840 mAh g^{-1}_S (cycle 50, sulfur from PS additive not included) comparable to R-E and E/S ratio of 6.5 μL_{R-E} mg^{-1}_S. Moreover, the CE is improved. Interestingly, the physicochemical properties of the electrolyte are not significantly affected when 0.2 M LiTFSI is substituted by 0.15 M Li_2S_6. At ambient conditions (20 – 30 °C) the ionic conductivity is only reduced by 1.9 – 2.0 mS cm^{-1} (Figure S4a), which is consistent with the increase in dynamic viscosity of 0.20 – 0.26 mPa s (Figure S4b) and limits detrimental effects solely to high rates. Also the structure of the DUT-107/S cathode (Figure 2) is not considerably affected by the substitution. More importantly, the densities of R-E and PS-E (Figure S4a inset) are almost the same meaning that for a given E/S ratio, the added PS (0.15 M Li_2S_6) does not increase the electrolyte weight in the assembled cell. In consequence, application of PS-E causes a real energy density boost on cell level, although the additional sulfur (in form of PS additive) was not included in the cathode capacity calculation.

These findings are supported by CV measurements of DUT-107/S cathodes in half cells with R-E (Figure 4a) and PS-E (Figure 4c), respectively. In agreement with the multi-step

conversion of sulfur to Li_2S_2/Li_2S and vice versa via long and short chain PS, two separated cathodic peaks at 2.23 – 2.42 V vs. Li/Li^+ (I; reduction of sulfur to long chain PS) and 2.00 – 2.10 V vs. Li/Li^+ (II; reduction of long chain PS to Li_2S_2/Li_2S) as well as one anodic peak at 2.20 – 2.45 V vs. Li/Li^+ (III; oxidation of Li_2S_2/Li_2S to sulfur via PS) are observed. The small shoulder of the anodic peak at 2.37 V vs. Li/Li^+ (IV) is discussed as a characteristic of sulfur confinement.[43] The small voltage gap between cathodic and anodic peaks evidences low polarization and, thus, not only fast kinetics but also good reversibility, although the DUT-107/S cathodes exhibit high sulfur content and loading. Interestingly, the zoom in of peak II (Figure 4a and 4c inset) reveals a decrease in specific current (measure for active material usability) for R-E compared to PS-E with increasing cycle number. This points towards an accumulation of short chain PS in the electrolyte (active material loss) during equilibration. This phenomenon can be suppressed by pre-saturation of the electrolyte with 0.15M Li_2S_6 (PS-E). Consequently, the peak II is stabilized and the specific current remains at a high level evidencing the effective compensation of active material loss without detrimental effects on the cathode performance, which is attributable to the well suited pore structure of DUT-107.

To characterize the degradation of DUT-107/S cathodes in more detail, EIS studies were performed for half cells in charged (2.6 V vs. Li/Li^+) and discharged (1.8 V vs. Li/Li^+) state in cycle 2 and 50 (Figure 4b and 4d), respectively. The Nyquist plots are composed of two depressed semicircles in the high and middle frequency domain as well as an inclined line in the low frequency region. Whereas the semicircle at high frequency associates with the SEI film covering the electrode surface (R_s), the semicircle in the middle frequency range indicates the charge transfer resistance (R_{ct}) resulting from the charge transfer through the electrode/electrolyte interface. The straight line at low frequency most likely associates with the solid-state diffusion of lithium ions into the electrode material. The intercept at the real axis (Z') at high frequency corresponds to the combination resistance (R_0), which consists of the ionic resistance of the electrolyte, the intrinsic resistance of the active materials and the

contact resistance at the active material/current collector interface.[4,44] In order to access the relevant resistance data, the spectra were fitted using a modified version of the equivalent circuit reported by Kolosnitsyn et al. (Figure S5 and Table S1).[4] The increase of R_0 over 50 cycles is most likely caused by a change of the ionic resistance due to PS dissolution. This can be deduced from measurements with R-E in both charged and discharged state, respectively, showing that R_0 increases from 0.96 and 0.13 to 3.29 and 3.17 Ω as cycling progresses. In contrast, the application of PS-E results in a stabilization of the combination resistance. R_0 remains constant at ca. 3.2 Ω in charged state and is increased from 0.93 to 2.77 Ω in discharged state indicating that equilibration was effectively induced by the pre-saturation. However, the contribution of the conductive framework (carbon material and active layer/current collector interface) degradation to the increase of R_0 is low. This can be attributed to the improved structural characteristics of DUT-107 allowing for reversible conversion of sulfur species inside the DUT-107 particles, thus achieving the long-lasting mechanical stability of the active layer. Interestingly, the initial R_{ct} is largely independent from the state-of-charge and the electrolyte used. Thus low values of 8.66 and 9.11 Ω were obtained in charged and discharged state, respectively, for R-E as well as 6.04 and 5.39 Ω for PS-E. However, upon cycling the semicircle in the middle frequency region grows and, accordingly, R_{ct} increases to 9.96 (charged state) and 19.74 Ω (discharged state) for R-E, which is less than the increase to 11.05 (charged state) and 30.61 Ω (discharged state) observed for PS-E. This phenomenon is caused by a loss of reaction sites due to PS leakage and irreversible precipitation of active material in the cell. In agreement with the significant increase of R_{ct} in discharged state, the formed layer blocking both electron and Li ion transport mainly consists of insulating Li_2S_2/Li_2S and becomes thicker as well as denser with increasing sulfur utilization as can be concluded from the measurement with PS-E. Interestingly, the structural characterization of DUT107/S cathodes revealed that layers

deposited on the DUT-107 particles in discharged state were effectively reutilized in the charge process due to the rational design of the DUT-107 pore structure. Therefore, the increase of R_{ct} is most likely caused by the continuous, irreversible deposition of high impedance layers on the lithium anode.

2.4. Electrochemical characterization of DUT-107/S cathodes in full cells (LiHC@GDL-S)

The problem of $LiNO_3$ consumption appears essential for all practicable types of sulfur cathodes and might only be circumvented by a fall back to thin films or high E/S ratios. However, both options largely decrease the energy density on cell level and are consequently not practical. Hence, the application of alternative anodes is a promising route for improved cell performance and high cycling stability.

In a full cell model system, a prelithiated hard carbon anode (LiHC@GDL) with stable areal capacity of ca. 3.0 mAh cm^{-2} (Figure S6a) was used as a substitute for the lithium anode and cycled vs. the DUT-107/S cathode with R-E (E/S = 12 μL_{R-E} mg$^{-1}_S$ to account for the anode porosity). In order to preserve a small excess of lithium, the full cell capacity was limited by the cathode areal capacity of ca. 2.9 mAh cm^{-2}. Interestingly, the cycling performance at 0.1 C is largely comparable for both full (Figure 5a) and half cell (Figure 3a). An initial capacity of 1268 mAh g$^{-1}_S$ was extracted from the DUT-107/S cathode, which stabilized at 813 mAh g$^{-1}_S$ after 24 cycles indicating that the electrolyte is saturated with PS in agreement with the corresponding half cell tests. Interestingly, the CE of the full cell decreased quickly although the SEI on LiHC@GDL is considered more stable than on elemental lithium. A reasonable explanation might be that the discharge cut-off voltage, which is difficult to define prior to the full cell tests, was adjusted too low leading to electrochemical $LiNO_3$ decomposition in agreement with observations in half cells.[45] Although the SEI formation on hard carbon in the Li-S system is not well understood yet, this draws attention to the fact that the SEI formed on

LiHC@GDL might not be dense enough to completely suppress the PS shuttle and thus continuously needs $LiNO_3$ for rebuilding. Nevertheless, detrimental effects such as lithium corrosion and electrolyte depletion are circumvented for this setup.[35] In combination with the improved characteristics of the mechanically stable active layer composed of DUT-107/S composite particles, ultralong cycling over 4100 cycles with a final reversible capacity of 422 mAh g^{-1}_S at 0.1 C is possible. This result corresponds to an overall capacity decay of only 48.1 % or 0.0118 % per cycle (over 4076 cycles), respectively, when related to the capacity of the equilibrated cell (cycle 24). To the best of our knowledge, this result surpasses all reports in the field in terms of long-lasting cyclability and capacity retention.[1,32,33,35,40] Moreover, the DUT-107/S cathode based full cell can operate at high rates of 0.5 C and 1 C, respectively, while maintaining reversible capacities of 591 mAh g^{-1}_S (cycle 200) and 365 mAh g^{-1}_S (cycle 1200). Due to the sloping potential of LiHC@GDL vs. Li/Li$^+$ (Figure S6b), the corresponding discharge voltage profiles (Figure 5b) are, especially in the lower plateau, slightly depressed compared to the half cells (Figure 3b). In contrast, the electrode kinetics are fast as can be deduced from the marginal voltage drop at rates of 0.5 C and 1 C, respectively. This is attributed not only to the hierarchical pore structure of DUT-107 allowing for fast mass transport and short PS diffusion length but also to the porous anode structure. The overall depression of the discharge voltage profiles with increasing cycle number is, most likely, caused by structural changes and surface layer formation degrading the electrical contacts in both cathode and anode.

To further verify the capacity stabilization by electrolyte pre-saturation, a full cell was measured with PS-E (12 μL_{PS-E} mg$^{-1}_S$) (Figure 5c). A much higher stable capacity of 1134 mAh g^{-1}_S is obtained in cycle 24 at 0.1 C, which subsequently degrades to 554 mAh g^{-1}_S in cycle 4100. This result corresponds to a capacity increase of 321 mAh g^{-1}_S (+ 39.5 %, sulfur from PS additive not included) after 24 cycles compared to R-E showing the functionality of the approach. Moreover, the capacity decay is still only 51.1 % or 0.0125 % per cycle (over

4076 cycles), respectively. The CE of the full cell with PS-E is higher compared to R-E, which is likely caused by the engagement of PS in the SEI formation on LiHC@GDL. Unfortunately, the capacity shows random fluctuations at a rate of 0.1 C. This might be attributed to the increase in cathode discharge capacity when using PS-E, which can suddenly invert the close balance between anode and cathode areal capacity and, thus, create a system that is temporarily anode limited. Since the cathode capacity is more sensitive to the applied current, these fluctuations vanish at high rates indicating that the obtainable anode capacity is again higher than the cathode capacity. Additionally, the performance at 1 C is lower for PS-E compared to R-E, which is a consequence of the lower ionic conductivity of PS-E. Accordingly, the discharge voltage profiles (Figure 5d) are well pronounced at a rate of 0.1 C and 0.5 C, but depressed at 1 C and after prolonged cycling when using PS-E.

In the CV curve of full cells measured with R-E (Figure 6a and S7a,b) and PS-E (Figure 6c and S7c,d), respectively, two cathodic peaks at 2.17 – 2.41 V (I) and 1.46 – 1.99 V (II) as well as one broad anodic peak at 1.56 – 2.46 V (III) are clearly visible. The shift of all peaks towards lower (cell) voltages as well as the considerable broadening of peak II and III is thereby caused by the sloping potential of LiHC@GDL. Interestingly, fluctuations are observed in the anodic peak (III) generating small, randomly occurring specific current maxima, whose origin was not studied yet. After cycling the full cell with R-E for as many as 4102 cycles, a constant shift of ca. 0.28 V towards lower cell potential as well as a large reduction of the specific current is clearly visible for all peaks indicating severe polarization and active material loss. This might be attributed to the leakage of PS from the DUT-107/S cathode leading to an increase of cell impedance, structural degradation and loss of electrical contact. Application of PS-E, in contrast, resulted in a slightly reduced shift of the cathodic peaks (I and II) of ca. 0.25 V indicating that the electrode kinetics are better preserved. Since the PS leakage is largely reduced by pre-saturation of PS-E, the drop of the specific current is much lower for PS-E compared to R-E highlighting that the sulfur utilization is still sufficient.

The EIS spectra of full cells measured with R-E (Figure 6b) and PS-E (Figure 6d), respectively, in cycle 2 and 4101 show features comparable to the half cell scans and were, therefore, fitted with the same equivalent circuit (Figure S5). Whereas the initial R_0 is only 2.91 and 2.42 Ω for R-E as well as 1.02 and 1.00 Ω for PS-E in charged and discharged state, respectively, an increase of R_0 to 7.05 and 5.97 Ω (R-E) as well as 9.26 and 8.95 Ω (PS-E) was observed in cycle 4101. This two- to three-fold increase compared to half cells in cycle 50 might not only be attributable to PS dissolution but also to loss of electrical contact as also indicated by the peak shift in the CV measurements. The evolution of R_{ct} in full cells is different from half cells. Whereas the initial R_{ct} is 16.03 and 12.52 Ω for R-E as well as 21.01 and 16.15 Ω for PS-E in charged and discharged state, respectively, it changes to 7.32 and 15.16 Ω (R-E) as well as 6.03 and 49.63 Ω (PS-E) in cycle 4101. On the one hand the increase of R_{ct} in discharged state evidences the formation of insulating surface layers on the cathode after prolonged cycling. However, this effect is only pronounced at very high sulfur utilization (PS-E). On the other hand the decrease of R_{ct} in charged state for both R-E and PS-E shows that, after initial activation (equilibration) of the DUT-107/S cathode, the charge transfer kinetics are improved. More importantly, the stabilization at low values in charged state points out the high reversibility of layer deposition leading to a long-lasting reutilization of Li_2S_2/Li_2S, which can be attributed to both the hierarchical pore system of DUT-107 and the circumvention of lithium degradation (continuous R_{ct} increase in half cells).

3. Conclusion

In this paper we demonstrated the application of DUT-107 as the carbon scaffold in the sulfur cathode for an advanced Li-S battery setup. DUT-107 exhibits high surface area (2088 m^2 g^{-1}), high total pore volume (3.17 cm^3 g^{-1}) and a multimodal hierarchical pore structure. This provides an excellent way for the preparation of mechanically stable DUT-107/S cathodes with sulfur content of 69.7 wt% per total electrode and sulfur loading of 2.3 – 2.9 mg_S cm^{-2}.

Close contact between electrochemical reaction sites (micro- and small mesopores located in the pore walls) and PS storage containers (large meso- and macropores) effectively shortens the diffusion length of active sulfur species and, thus, preserves fast reaction kinetics even at E/S ratios of 5.0 μL_{R-E} mg^{-1}$_S$. Although initial capacities in range of 1098 to 1208 mAh g^{-1}$_S$ were obtained almost independently from the E/S ratio, a significant impact on the capacity retention as well as the achievable cycle number was observed as a result of PS leakage, LiNO$_3$ consumption and electrolyte depletion. Whereas substitution of 0.2 M LiTFSI conducting salt by 0.15M Li$_2$S$_6$ additive (pre-saturation of electrolyte) resulted in reduced active material loss and capacity stabilization, the physicochemical properties of the electrolyte were not significantly affected. Even after substitution of elemental lithium by LiHC@GDL, the excellent performance of DUT-107/S cathodes was reproducible. Moreover, the capacity decay was significantly reduced to only 0.0118 % per cycle allowing a final capacity of 422 mAh g^{-1}$_S$ after 4100 cycles. Moreover, application of PS additive resulted in a further performance increase (final capacity of 554 mAh g^{-1}$_S$), but slightly higher decay of 0.0125 % per cycle.

4. Experimental Section

Template synthesis: The silica-template was prepared similar to the sol-gel method reported by Smått et al.[46] First poly(ethylene glycol) (PEG 1500; M$_w$ ≈ 1500 g mol^{-1}; Acros Organics) and hexadecyltrimethylammonium bromide (CTAB; Acros Organics) were diluted in a mixture of water and concentrated nitric acid (HNO$_3$; ≥ 65 %; Sigma Aldrich) and stirred until a clear solution was obtained. After adding tetraethoxysilane (TEOS; Aldrich) the mixture was homogenized for 30 min. The molar ratio of PEG 1500 / CTAB / TEOS / HNO$_3$ / H$_2$O was 0.00103 / 0.014 / 1.00 / 0.0125 / 1.47. After aging for 72 h at 40 °C, the obtained gel was stirred in 2 M ammonia solution (NH$_3$; Aldrich) for 24 h at 90 °C to strengthen the silica

structure.[47] The product was washed thoroughly with deionized water and ethanol and calcinated at 550 °C for 5 h in air.

DUT-107 synthesis: The silica-template was infiltrated with polycarbosilane (PCS; $M_w \approx 800$ g mol^{-1}; Aldrich) as reported elsewhere.[37] For the infiltration of 1 g PCS a mixture of 24 mL heptane (Alfa Aesar) and 0.14 mL butanol (Alfa Aesar) was used. After evaporation of the infiltration solution overnight, the powder was converted into a $SiC-SiO_2$-ceramic by pyrolysis in a horizontal tubular furnace under argon atmosphere at 1000 °C. The following regime was used: (1) heating from room temperature to 300 °C, ramp = 150 °C h^{-1}, (2) heat treatment at 300 °C for 5 h, (3) heating to 700 °C, ramp = 30 °C h^{-1}, (4) heating to 1000 °C, ramp = 120 °C h^{-1}, (5) pyrolysis at 1000 °C for 2 h and (6) cooling to room temperature. The $SiC-SiO_2$-ceramic was etched with a mixture of hydrofluoric acid, ethanol and deionized water (1:1:1 by volume) for 12 h to extract the silica-template. The washed SiC was transformed into a carbide-derived carbon (CDC, DUT-107) by chlorine etching at 1000 °C for 3 h in a gas flow of 80 mL min^{-1} chlorine and 70 mL min^{-1} argon. Afterwards the furnace was cooled down to 600 °C under argon flow for a final 1 h hydrogen treatment (removal of chlorine residues).

Composite preparation: DUT-107 and sulfur ($\geq$ 99.5 %; Sigma Aldrich) were combined in a mortar in a ratio of 1:4 (by weight) and thoroughly milled. The homogeneous powder was transferred into a porcelain crucible and heat treated at 155 °C for 12 h in air to allow the melt infiltration sulfur in the pores of DUT-107.

Cathode preparation: A cathode film was prepared from the DUT-107/S powder following a solvent-free roll pressing procedure.[30] In order to maximize the sulfur content in the cathode and improve the wettability of the active layer, the ratio of DUT-107/S, multi-walled carbon nanotube (MWCNT; > 95 %; Baytubes C 70 P; Bayer MaterialScience) conductive additive and polytetrafluoroethylene (PTFE; Aldrich) binder was slightly altered to 85:12:3 (by weight). The cathode film was laminated onto a one-sided primer-coated, expanded aluminum

(99.5%; Benmetal – Bender GmbH) current collector. Circular electrodes (Ø 12 mm) with a typical sulfur loading of 2.3 – 2.9 mg_S cm^{-2} were punched and used without further treatment.

Hard carbon anode preparation: A slurry containing 90 wt% commercial hard carbon powder (HC; Carbotron P; Kureha GmbH), 5 wt% MWCNT and 5 wt% styrene butadiene rubber (SBR; 15 wt% in water; Targray) was pressed into a commercial carbon non-woven (GDL; GDL Y0200; Freudenberg). After drying overnight circular HC@GDL electrodes (Ø 15 mm) with a typical weight of 12.6 – 13.6 mg cm^{-2} were punched and used without further treatment.

Electrolyte preparation: The reference electrolyte (R-E) was prepared by dissolving lithium bis(trifluoromethylsulfonyl)imide (LiTFSI; 99.95 %; Sigma Aldrich) and lithium nitrate ($LiNO_3$; 99.98 %; anhydrous; Alfa Aesar) in a mixture (1:1 by volume) of 1,2-dimethoxyethane (DME; 99.5 %; anhydrous; H_2O < 20 ppm; Sigma Aldrich) and 1,3-dioxolane (DOL; 99.8 %; anhydrous; H_2O < 20 ppm; Sigma Aldrich). The concentration was 1 M LiTFSI + 0.25 M $LiNO_3$. For the preparation of polysulfide electrolyte (PS-E), lithium (Kyokuto Metal (HK) Ltd) and sulfur were combined in a stoichiometric ratio of 2:6 and rigorously stirred in a mixture (1:1 by volume) of DME and DOL for 4 days at room temperature. The 0.2 M Li_2S_6 stock solution was mixed with LiTFSI, $LiNO_3$ and DME/DOL to adjust the electrolyte composition of 0.8 M LiTFSI + 0.25 M $LiNO_3$ + 0.15 M Li_2S_6. LiTFSI and $LiNO_3$ salt were dried before use. DME and DOL were dried and stored over molecular sieve 3 Å. The work was carried out in an argon glove box (H_2O and O_2 < 0.1 ppm).

Cell assembly: CR2016 coin cells (MTI Corp) were assembled in an argon glove box by stacking the DUT-107/S cathode (working electrode), one layer of Celgard 2500 separator and the anode (counter and reference electrode). In half cells a lithium chip (Ø 15.6 mm; 99.0 %; PI-KEM Ltd) was used as anode, whereas in full cells lithium was substituted by prelithiated HC@GDL (LiHC@GDL). Before crimping a defined amount of R-E and PS-E,

respectively, was added to the cells. In the prelithiation step HC@GDL was cycled as cathode vs. lithium.

Structural characterization: To analyze the micro- and mesopores of DUT-107 and DUT-107/S nitrogen physisorption measurements were performed at -196 °C using a Quantachrome QUADRASORB apparatus. Whereas DUT-107 was degassed at 150 °C in vacuum, the DUT-107/S composite was activated at room temperature in vacuum to minimize sulfur sublimation. The specific surface area (SSA) of DUT-107 was calculated according to the multipoint Brunauer-Emmett-Teller (MPBET) equation in a p/p_0 range of 0.07 – 0.3. Pore size distributions (PSD) of DUT-107 and DUT-107/S were calculated using the quenched solid density functional theory (QSDFT) for nitrogen (-196 °C) on carbon. For comparability the isotherm and PSD of DUT-107/S were recalculated based on the DUT-107 content in the composite. The micropore volume of DUT-107 was derived from the cumulative pore volume at d_P = 2 nm. To analyze the meso- and macropores of DUT-107 mercury (HG) intrusion porosimetry was performed using a Micromeritics AutoPore IV 9500 (V1.07) apparatus. The HG-PSD was calculated according to ISO 15901-1 instruction. The total pore volume of DUT-107 was determined by combining nitrogen physisorption (cumulative pore volume at d_P = 5.56 nm) and mercury intrusion (mercury volume intruded for $d_P \leq$ 192.29 nm) data. The cathode structure was analyzed by X-ray diffraction (XRD) on a Siemens D5005 diffractometer with Cu-Kα radiation (λ = 0.154 nm). A JEOL JEM-2100 transmission electron microscope (TEM) was employed for pore structure studies. The morphology of cathodes was analyzed on a JEOL JSM-7800F scanning electron microscope (SEM) using secondary electron (SE) and backscattered electron (BSE) detectors, respectively. The distribution of sulfur and carbon was characterized using the equipped Oxford energy dispersive X-ray spectroscopy (EDX) detector. Cycled cathodes were analyzed on a JEOL JSM-6610LV SEM with minimal air contact during sample transfer. The sulfur content of the DUT-107/S composite was determined via thermogravimetric (TG) analysis using a Netzsch

STA 409 PC Luxx apparatus. Synthetic air was used as carrier gas and the temperature was increased from room temperature to 900 °C with a ramp of 5 °C min^{-1}.

Cathode recovery: Coin cells cycled at 0.1 C for 10 cycles were immediately disassembled in an argon glove box. The cathodes were collected and intensively washed with DOL to remove residual polysulfides. After drying, one part of each sample was stored for SEM studies, whereas the other part was sealed air-tight under Kapton-Tape for XRD characterization.

Electrolyte characterization: Ionic conductivities were measured with a Knick 703 conductometer from 50 to -20 °C. After calibration with 0.1 M NaCl solution at 20 °C, the cell was filled with electrolyte and sealed under argon atmosphere. The temperature was adjusted with a Julabo F 32 thermostat. Viscosity and density measurements were performed using a Stabinger SVM 3000 viscometer with integrated thermostat from 50 to -20 °C.

Electrochemical investigation of half cells: Constant current (CC) cycling of DUT-107/S cathodes vs. lithium was performed using a BASYTEC CTS system. All half cells were operated at a rate of 0.1 C (1 C = 1672 mA g$^{-1}_S$) in a voltage range of 1.8 – 2.6 V vs. Li/Li$^+$. Electrochemical impedance spectroscopy (EIS) and cyclic voltammetry (CV) were performed using an IVIUM N-STAT multichannel potentiostat. The EIS spectra were collected in cycle 2 and 50, respectively, for cells in discharged (1.80 V vs. Li/Li$^+$) as well as charged (2.60 V vs. Li/Li$^+$) state (frequency range: 100 kHz – 0.1 Hz; AC amplitude: 10 mV). The CV measurements were performed in a voltage range of 1.8 – 2.6 V vs. Li/Li$^+$ (sweep rate: 20 µV s^{-1}). Temperature conditions: 23 – 25 °C.

Electrochemical investigation of full cells: Constant current (CC) cycling of DUT-107/S cathodes vs. LiHC@GDL was performed in a cell voltage range of 0.8 – 2.6 V using the following protocol: 100 cycles at 0.1 C, 900 cycles at 0.5 C, 50 cycles at 0.1 C, 3000 cycles at 1 C and 50 cycles at 0.1 C. For the prelithiation of HC@GDL the following constant current-constant voltage (CC-CV) protocol was applied: CC discharge at 0.5 mA cm^{-2} to a voltage of 10 mV vs. Li/Li$^+$ plus CV step to a current of 0.064 mA cm^{-2} and subsequent CC charge at 0.5

mA cm^{-2} to a voltage of 1.5 V vs. Li/Li$^+$ for 5 cycles, followed by a final CC-CV discharge. The EIS spectra were collected in cycle 2 and 4101, respectively, for cells in discharged (cell voltage of 0.80 V) as well as charged (cell voltage of 2.60 V) state. The cyclic voltammetry (CV) measurements were performed in a cell voltage range of 0.8 – 2.6 V. For EIS, CV and temperature conditions see above.

Additional Information: Electronic Supplementary Information is available online.

**References**

1   M.-K. Song, Y. Zhang and E. J. Cairns, *Nano Lett.*, 2013, **13**, 5891–5899.

2   M. Hagen, P. Fanz and J. Tübke, *J. Power Sources*, 2014, **264**, 30–34.

3   a) R. Rauh, F. Shuker, J. Marston and S. Brummer, *J. Inorg. Nucl. Chem.*, 1977, **39**, 1761–1766; b) V. S. Kolosnitsyn, E. V. Karaseva, D. Y. Seung and M. D. Cho, *Russ. J. Electrochem.*, 2002, **38**, 1314–1318; c) W. Wang, Y. Wang, Y. Huang, C. Huang, Z. Yu, H. Zhang, A. Wang and K. Yuan, *J. Appl. Electrochem.*, 2010, **40**, 321–325.

4   V. Kolosnitsyn, E. Kuzmina, E. Karaseva and S. Mochalov, *J. Power Sources*, 2011, **196**, 1478–1482.

5   a) WO Patent 2007/034243, 2007; b) J.-W. Choi, J.-K. Kim, G. Cheruvally, J.-H. Ahn, H.-J. Ahn and K.-W. Kim, *Electrochim. Acta*, 2007, **52**, 2075–2082.

6   X. Ji, K. T. Lee and L. F. Nazar, *Nat. Mater.*, 2009, **8**, 500–506.

7   Y. Diao, K. Xie, S. Xiong and X. Hong, *J. Electrochem. Soc.*, 2012, **159**, A421–A425.

8   Y. V. Mikhaylik, I. Kovalev, R. Schock, K. Kumaresan, J. Xu and J. Affinito, *ECS Trans.*, 2010, **25**, 23–34.

9   a) Y. V. Mikhaylik and J. R. Akridge, *J. Electrochem. Soc.*, 2004, **151**, A1969–A1976; b) X. Ji and L. F. Nazar, *J. Mater. Chem.*, 2010, **20**, 9821–9826.

10 V. S. Kolosnitsyn and E. V. Karaseva, *Russ. J. Electrochem.*, 2008, **44**, 506–509.

11 J. Zheng, D. Lv, M. Gu, C. Wang, J.-G. Zhang, J. Liu and J. Xiao, *J. Electrochem. Soc.*, 2013, **160**, A2288–A2292.

12 R. Elazari, G. Salitra, Y. Talyosef, J. Grinblat, C. Scordilis-Kelley, A. Xiao, J. Affinito and D. Aurbach, *J. Electrochem. Soc.*, 2010, **157**, A1131–A1138.

13 S.-E. Cheon, S.-S. Choi, J.-S. Han, Y.-S. Choi, B.-H. Jung and H. S. Lim, *J. Electrochem. Soc.*, 2004, **151**, A2067–A2073.

14 B. H. Jeon, J. H. Yeon, K. M. Kim and I. J. Chung, *J. Power Sources*, 2002, **109**, 89–97.

15 V. Kolosnitsyn, E. Kuzmina and S. Mochalov, *J. Power Sources*, 2014, **252**, 28–34.

16 F. Orsini, A. Du Pasquier, B. Beaudoin, J. Tarascon, M. Trentin, N. Langenhuizen, E. de Beer and P. Notten, *J. Power Sources*, 1998, **76**, 19–29.

17 M. Hagen, G. Feisthammel, P. Fanz, H. T. Grossmann, S. Dörfler, J. Tübke, M. J. Hoffmann, D. Börner, M. Joos, H. Althues and S. Kaskel, *J. Electrochem. Soc.*, 2013, **160**, A996–A1002.

18 J. Brückner, S. Thieme, H. T. Grossmann, S. Dörfler, H. Althues and S. Kaskel, *J. Power Sources*, 2014, **268**, 82–87.

19 S. Zhang, *Energies*, 2012, **5**, 5190–5197.

20 S. Urbonaite and P. Novák, *J. Power Sources*, 2014, **249**, 497–502.

21 a) B. Zhang, X. Qin, G. R. Li and X. P. Gao, *Energy Environ. Sci.*, 2010, **3**, 1531–1537; b) R. Elazari, G. Salitra, A. Garsuch, A. Panchenko and D. Aurbach, *Adv. Mater.*, 2011, **23**, 5641–5644; c) M. Rao, W. Li and E. J. Cairns, *Electrochem. Commun.*, 2012, **17**, 1–5; d) W. Zhang, D. Qiao, J. Pan, Y. Cao, H. Yang and X. Ai, *Electrochim. Acta*, 2013, **87**, 497–502.

22 C. Liang, N. J. Dudney and J. Y. Howe, *Chem. Mater.*, 2009, **21**, 4724–4730.

23 G. He, X. Ji and L. Nazar, *Energy Environ. Sci.*, 2011, **4**, 2878–2883.

24 J. Schuster, G. He, B. Mandlmeier, T. Yim, K. T. Lee, T. Bein and L. F. Nazar, *Angew. Chem. Int. Ed.*, 2012, **51**, 3591–3595.

25 G. Xu, B. Ding, P. Nie, L. Shen, H. Dou and X. Zhang, *ACS Appl. Mater. Interfaces*, 2014, **6**, 194–199.

26 B. Ding, C. Yuan, L. Shen, G. Xu, P. Nie and X. Zhang, *Chem. Eur. J.*, 2013, **19**, 1013–1019.

27 M. Oschatz, S. Thieme, L. Borchardt, M. R. Lohe, T. Biemelt, J. Brückner, H. Althues and S. Kaskel, *Chem. Commun.*, 2013, **49**, 5832–5834.

28 M. Oschatz, L. Borchardt, K. Pinkert, S. Thieme, M. R. Lohe, C. Hoffmann, M. Benusch, F. M. Wisser, C. Ziegler, L. Giebeler, M. H. Rümmeli, J. Eckert, A. Eychmüller and S. Kaskel, *Adv. Energy Mater.*, 2014, **4**, 1300645.

29 J. T. Lee, Y. Zhao, S. Thieme, H. Kim, M. Oschatz, L. Borchardt, A. Magasinski, W. I. Cho, S. Kaskel and G. Yushin, *Adv. Mater.*, 2013, **25**, 4573–4579.

30 S. Thieme, J. Brückner, I. Bauer, M. Oschatz, L. Borchardt, H. Althues and S. Kaskel, *J. Mater. Chem. A*, 2013, **1**, 9225–9234.

31 X. Wang, X. Fang, X. Guo, Z. Wang and L. Chen, *Electrochim. Acta*, 2013, **97**, 238–243.

32 Z. W. Seh, W. Li, J. J. Cha, G. Zheng, Y. Yang, M. T. McDowell, P.-C. Hsu and Y. Cui, *Nat. Commun.*, 2013, **4**, 1331.

33 S. Lu, Y. Cheng, X. Wu and J. Liu, *Nano Lett.*, 2013, **13**, 2485–2489.

34 a) R. Elazari, G. Salitra, G. Gershinsky, A. Garsuch, A. Panchenko and D. Aurbach, *Electrochem. Commun.*, 2012, **14**, 21–24; b) Y. Yang, M. T. McDowell, A. Jackson, J. J. Cha, S. S. Hong and Y. Cui, *Nano Lett.*, 2010, **10**, 1486–1491; c) J. Hassoun, J. Kim, D.-J. Lee, H.-G. Jung, S.-M. Lee, Y.-K. Sun and B. Scrosati, *J. Power Sources*, 2012, **202**, 308–313; d) M. Hagen, E. Quiroga-González, S. Dörfler, G. Fahrer, J. Tübke, M. Hoffmann, H. Althues, R. Speck, M. Krampfert, S. Kaskel and H. Föll, *J. Power Sources*, 2014, **248**, 1058–1066; e) J. Hassoun and B. Scrosati, *Angew. Chem. Int. Ed.*, 2010, **49**, 2371–2374.

35 J. Brückner, S. Thieme, F. Böttger-Hiller, I. Bauer, H. T. Grossmann, P. Strubel, H. Althues, S. Spange and S. Kaskel, *Adv. Funct. Mater.*, 2014, **24**, 1284–1289.

36 M. Oschatz, E. Kockrick, M. Rose, L. Borchardt, N. Klein, I. Senkovska, T. Freudenberg, Y. Korenblit, G. Yushin and S. Kaskel, *Carbon*, 2010, **48**, 3987–3992.

37 P. Krawiec, E. Kockrick, L. Borchardt, D. Geiger, A. Corma and S. Kaskel, *J. Phys. Chem. C*, 2009, **113**, 7755–7761.

38 a) L.-X. Miao, W.-K. Wang, A.-B. Wang, K.-G. Yuan and Y.-S. Yang, *J. Mater. Chem. A*, 2013, **1**, 11659–11664; b) M. Wang, W. Wang, A. Wang, K. Yuan, L. Miao, X. Zhang, Y. Huang, Z. Yu and J. Qiu, *Chem. Commun.*, 2013, **49**, 10263–10265.

39 S. S. Zhang and J. A. Read, *J. Power Sources*, 2012, **200**, 77–82.

40 Z. W. Seh, Q. Zhang, W. Li, G. Zheng, H. Yao and Y. Cui, *Chem. Sci.*, 2013, **4**, 3673–3677.

41 a) C.-N. Lin, W.-C. Chen, Y.-F. Song, C.-C. Wang, L.-D. Tsai and N.-L. Wu, *J. Power Sources*, 2014, **263**, 98–103; b) J. Nelson, S. Misra, Y. Yang, A. Jackson, Y. Liu, H. Wang, H. Dai, J. C. Andrews, Y. Cui and M. F. Toney, *J. Am. Chem. Soc.*, 2012, **134**, 6337–6343.

42 a) S. Chen, F. Dai, M. L. Gordin and D. Wang, *RSC Adv.*, 2013, **3**, 3540–3543; b) R. Xu, I. Belharouak, J. C. M. Li, X. Zhang, I. Bloom and J. Bareño, *Adv. Energy Mater.*, 2013, **3**, 833–838.

43 Y. Fu, Y.-S. Su and A. Manthiram, *ACS Appl. Mater. Interfaces*, 2012, **4**, 6046–6052.

44 a) J. Xie, J. Yang, X. Zhou, Y. Zou, J. Tang, S. Wang and F. Chen, *J. Power Sources*, 2014, **253**, 55–63; b) M. Rao, X. Song and E. J. Cairns, *J. Power Sources*, 2012, **205**, 474–478.

45 S. S. Zhang, *Electrochim. Acta*, 2012, **70**, 344–348.

46 J.-H. Smått, S. Schunk and M. Lindén, *Chem. Mater.*, **15**, 2354–2361.

47 A.-H. Lu, J.-H. Smått, S. Backlund and M. Lindén, *Micropor. Mesopor. Mat.*, 2004, **72**, 59–65.
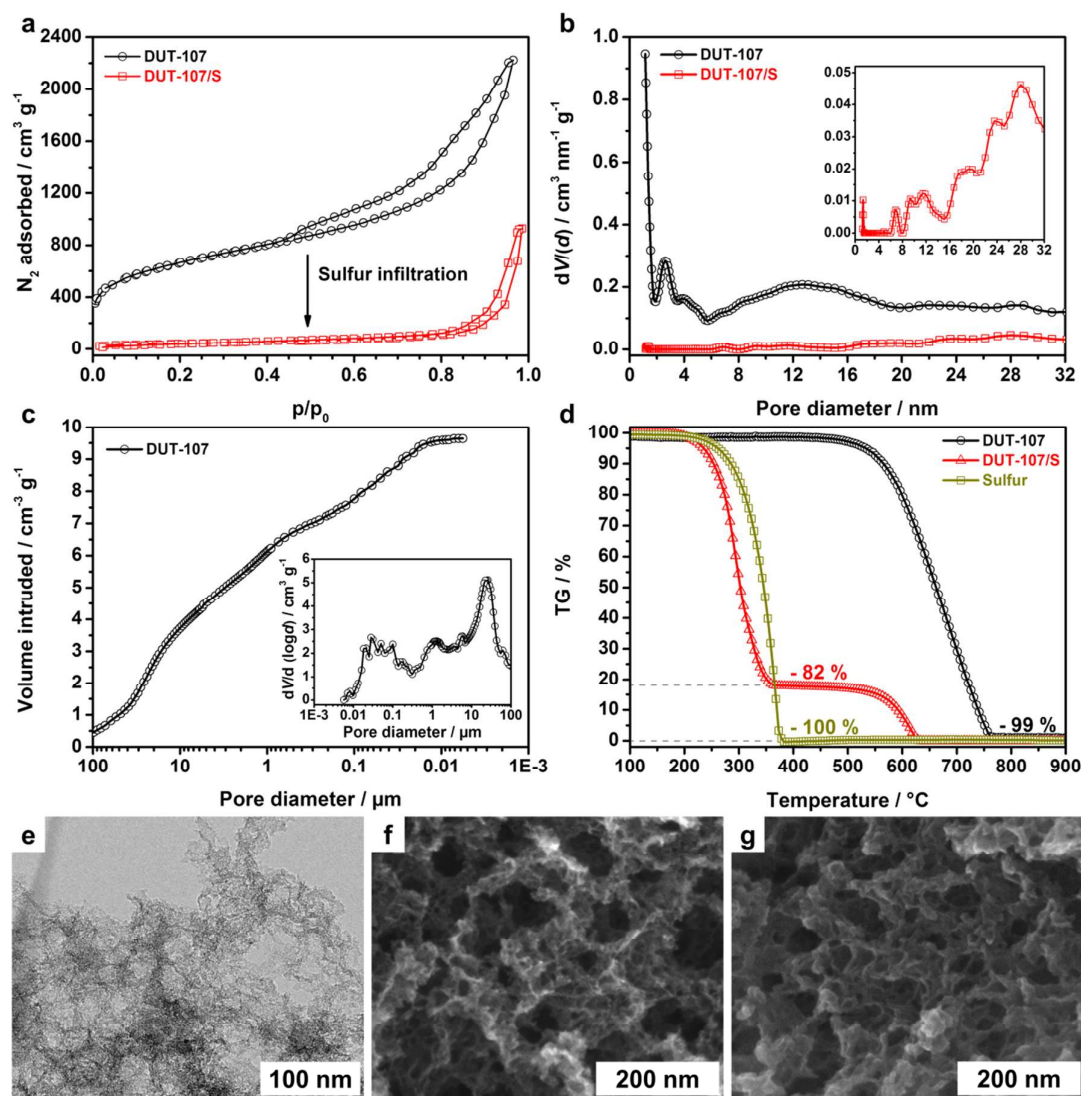
Figure 1. (a) Nitrogen physisorption (-196 °C) isotherms of DUT-107 and DUT-107/S. The isotherm of the composite was recalculated based on the DUT-107 content in DUT-107/S for comparability. (b) Nitrogen physisorption PSD of DUT-107 and DUT-107/S. The inset shows the magnified curve of DUT-107/S. (c) Mercury intrusion porosimetry of DUT-107. The inset shows the corresponding HG-PSD. (d) TG analysis of DUT-107, pristine sulfur and DUT-107/S in synthetic air atmosphere. (e,f) Representative TEM and SEM image of DUT-107. (g) SEM image of the DUT-107/S composite.
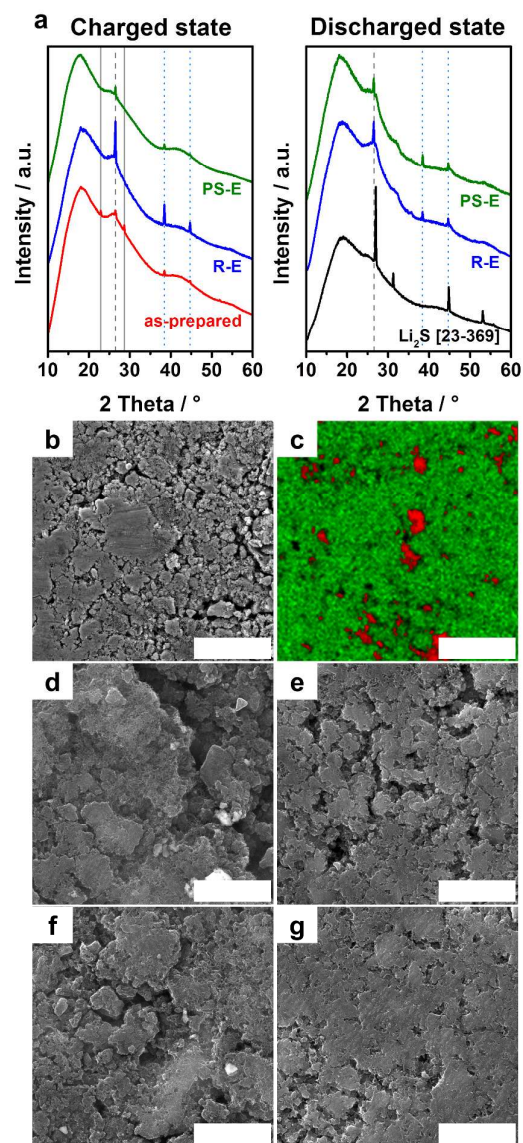
Figure 2. (a) XRD pattern of the as-prepared DUT-107/S cathode as well as cathodes cycled with R-E and PS-E in charged and discharged state, respectively. Vertical lines correspond to sulfur (solid), graphite (dashed) and primer-coated aluminum current collector (dotted). (b,c) SEM image and EDX elemental map (red = carbon, green = sulfur) of the as-prepared cathode. (d,e) SEM images of cathodes cycled with R-E in charged and discharged state. (f,g) SEM images of cathodes cycled with PS-E in charged and discharged state. Scale bars: 10 μm.
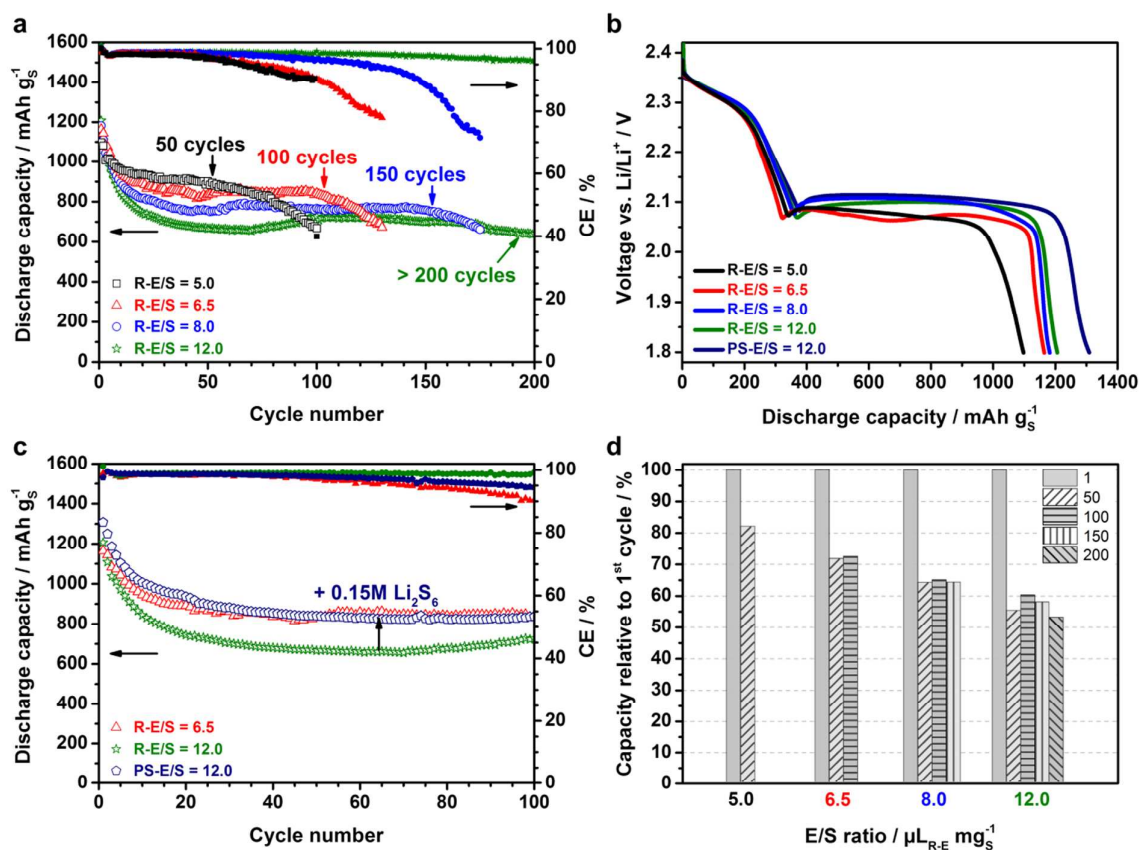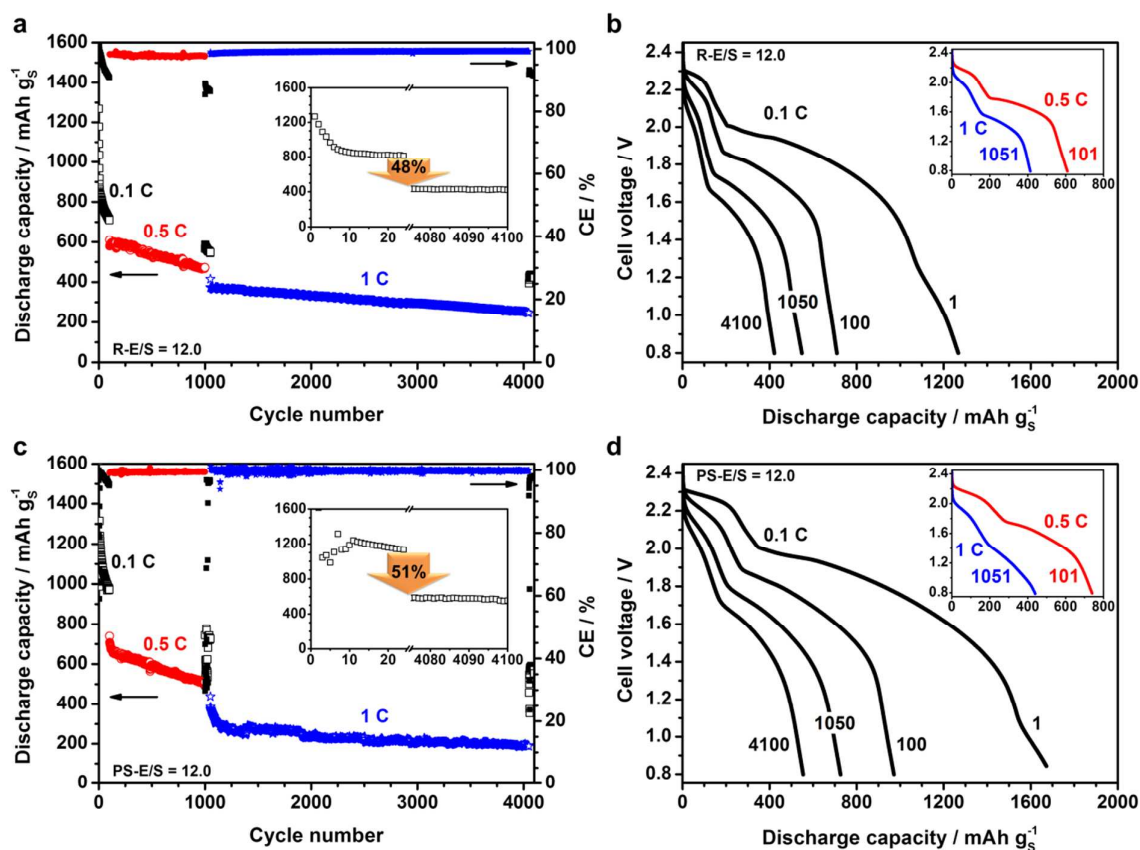
Figure 3. (a,b) Cycling performance and corresponding 1st cycle discharge voltage profiles of DUT-107/S cathodes measured with R-E (E/S = 5.0 – 12.0 μL$_{R-E}$ mg^{-1}$_S$) in half cells (vs. lithium) at 0.1 C. (c) Cycling performance of a DUT-107/S cathode measured with PS-E (E/S = 12.0 μL$_{PS-E}$ mg^{-1}$_S$) in half cell at 0.1 C. (d) Capacity retention of DUT-107/S cathodes cycled with R-E.

31
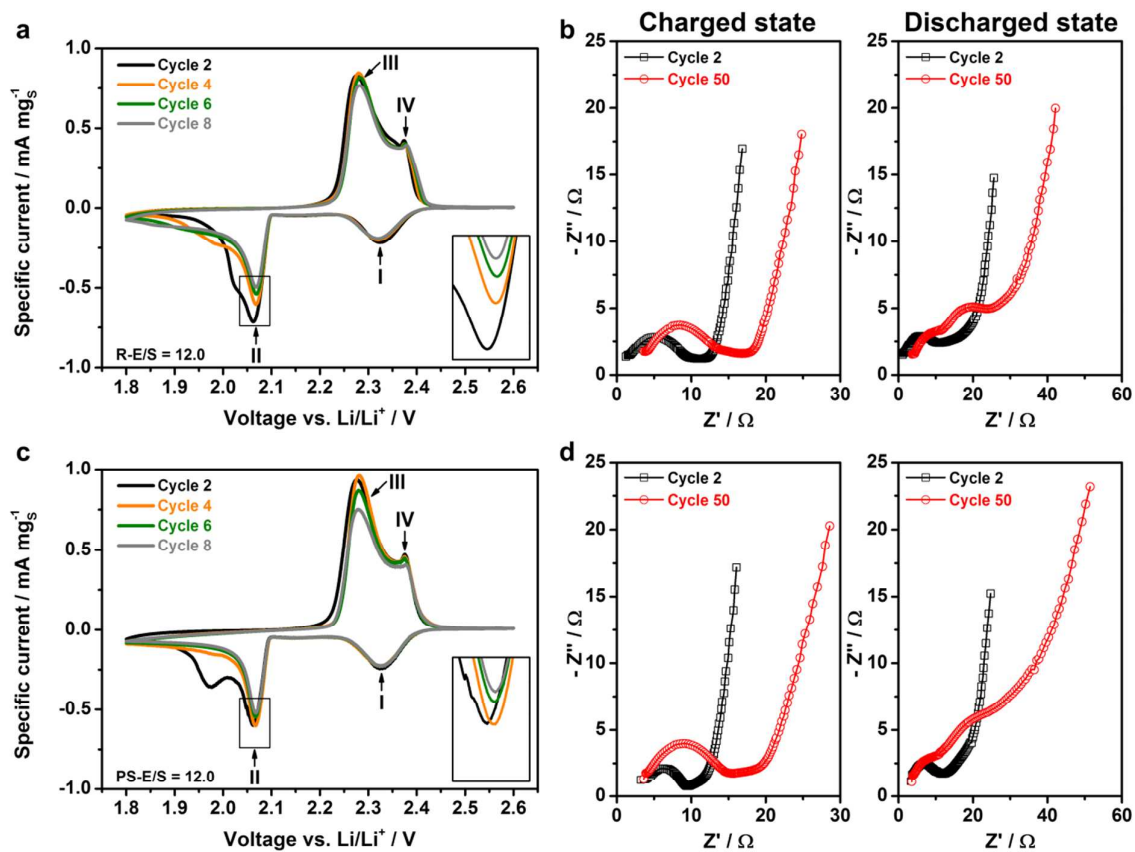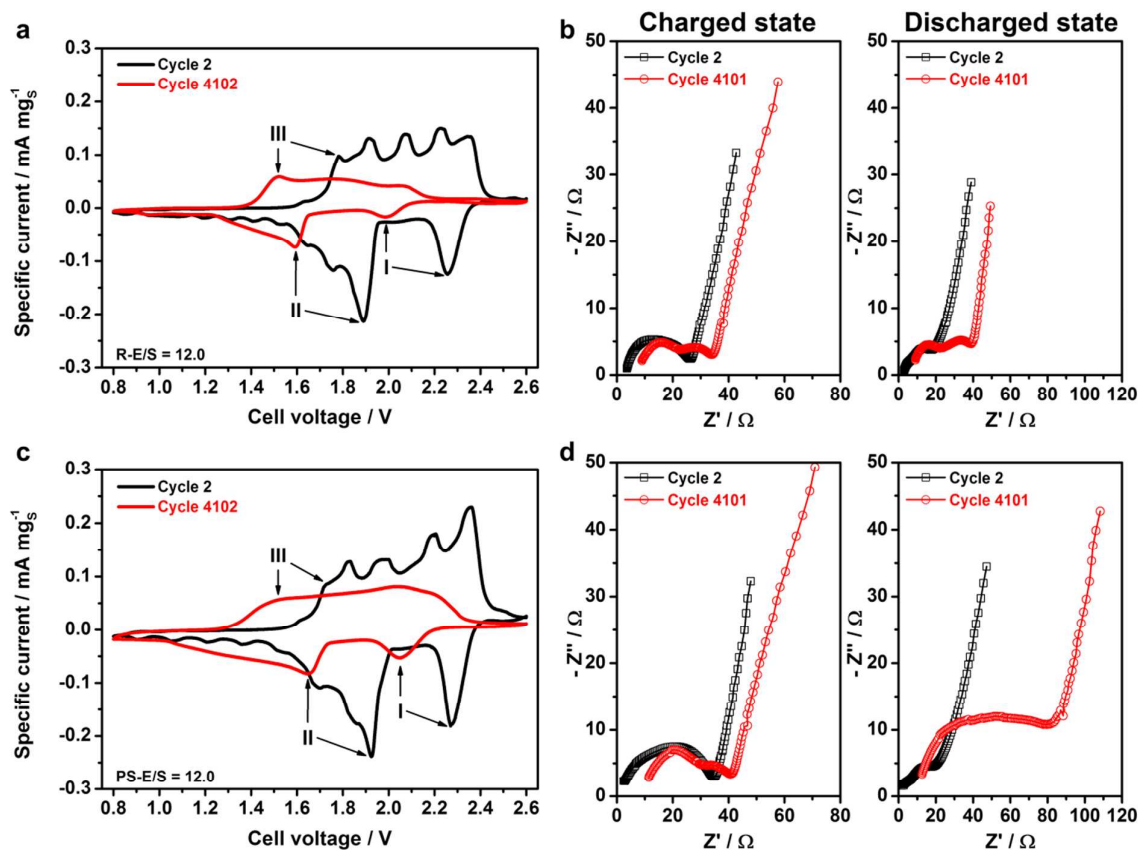
Figure 4. CV and Nyquist plots of DUT-107/S cathodes measured in half cells (vs. lithium) with 12.0 μL_E mg^{-1}$_S$. The electrolyte was R-E (a,b) and PS-E (c,d), respectively. The insets show a magnification of cathodic peak II. The EIS scans were performed in charged and discharged state, respectively.

Figure 5. Cycling performance and corresponding discharge voltage profiles of DUT-107/S cathodes measured in full cell setup (vs. LiHC@GDL) with 12.0 μL_E mg^{-1}$_S$ at alternating rate. The electrolyte was R-E (a,b) and PS-E (c,d), respectively. The insets in the cycling experiments compare the initial (cycle 1 – 24) and final (cycle 4076 – 4100) discharge capacities at 0.1 C.

Figure 6. CV and Nyquist plots of DUT-107/S cathodes measured in full cell setup (vs. LiHC@GDL) with 12.0 μL_E mg^{-1}_S. The electrolyte was R-E (a,b) and PS-E (c,d), respectively. The EIS scans were performed in charged and discharged state, respectively.